JOURNAL OF GEOPHYSICAL RESEARCH, VOL. 102, NO. C8, PAGES 18,661–18,680, AUGUST 15, 1997

Flow dynamics of a wide Arctic canyon

S. R. Signorini,[1] A. Münchow, and D. Haidvogel
Institute of Marine and Coastal Sciences, Rutgers University, New Brunswick, New Jersey

Abstract. We extend and interpret acoustic Doppler current profiler and conductivity-temperature-depth data collected in the summer of 1993 over Barrow Canyon in order to implement a high resolution (1.5 to 5 km) model of the Beaufort and Chukchi Seas. This paper addresses physical processes relevant to the Barrow Canyon region using common dynamical analyses of both field data and numerical results. The field data reveal the dominant physical processes that guide the design of our numerical experiments. The observed velocity field shows an intense and variable down canyon flow with transports ranging from 0.5 to 1.4 Sv. A momentum analysis reveals that the cross-canyon dynamic balance for the barotropic component is primarily geostrophic. Conversely, the baroclinic cross-canyon momentum balance is ageostrophic and secondary flow results from a local imbalance between the vertically varying Coriolis acceleration and the cross-canyon pressure gradient. In addition to the moderate influence of stratification (Froude number of 0.4 and Burger number of 0.06), the barotropic pressure gradient component across the canyon (inferred from the large magnitude and little vertical variability of the residuals) is dynamically important for both upcanyon and downcanyon flows that occur at different locations concurrently. The along-canyon dynamic balance is ageostrophic since the time derivative and the Coriolis term are of the same order of magnitude (temporal Rossby number is approximately 1). An analysis of the longitudinal density and velocity fields from the model reveals that the main driving mechanism for generating the observed upcanyon flow is the nonlinear interaction of the variable barotropic flow with the steep topography. Stratification is maintained by the downcanyon advection of fresh and warm water from the Bering and Chukchi Seas and the upcanyon advection of saltier and colder water from the Arctic.

1. Introduction

In the Arctic Ocean one often finds much enhanced currents near topographic features such as ridges, channels, canyons, islands, and shelf breaks [*Aagaard*, 1989; *Kowalik and Proshutinsky*, 1995]. The dynamic regimes near topographic slopes affect and partly drive the generally weak circulation of the Arctic Ocean. The thermohaline circulation within the Arctic Ocean in turn impacts both global climate [*Aagaard and Carmack*, 1994] and the large scale circulation of the Atlantic Ocean [*Dickson et al.* 1988]. The Arctic Ocean is characterized by large variations in albedo because of the ever changing ice cover, dense water formation due to freezing and subsequent brine rejection [*Melling*, 1993], large amounts of riverine freshwater discharge that are exported into the Atlantic in the form of ice [*Aagaard and Carmack*, 1989], and interaction and mixing of Atlantic and Pacific waters (A. Münchow and E. Carmack, Synoptic flow and density observations in a wide Arctic canyon, submitted to *J. Phys. Oceanogr.*, 1997)(hereinafter referred to as Münchow and Carmack, submitted manuscript, 1997). *Aagaard* [1989] and *Aagaard and Carmack* [1994] review much of the presently available Arctic current meter data. Direct velocity observations in the Arctic Ocean are spotty at best. Hence, numerical circulation studies such as *Holland et al.* [1996] constitute an important tool in the assessment of the Arctic circulation and that of the adjacent North Atlantic Ocean.

Most ice-ocean general circulation models are forced by observed or idealized climatological wind and density fields. They generally have horizontal resolutions larger than 80 km. Thus they resolve neither the internal deformation radius nor the steep topography. Furthermore, present basin scale models are incapable of adequately resolving the vast Arctic continental shelves and many baroclinic processes that are important there [*Gawarkiewicz and Chapman*, 1995]. Continental shelves constitute about a third of the entire surface area of the Arctic Ocean and are in some places more than 800 km wide. The circulation on Arctic shelves is generally more dynamic than in the deep Arctic Ocean as

[1]Now at General Sciences Corporation, Laurel, Maryland.

Paper number 97JC00739.
0148-0227/97/97JC-00739$09.00

they are exposed to direct atmospheric forcing during the 2-4 months long ice free summer season. In this paper we study, both numerically and observationally, the dynamics of a small region of the Arctic Ocean where the shelf circulation interacts vigorously with the circulation over the continental slope and the deep basin. In our study of the 30-km-wide Barrow Canyon we use an idealized, high-resolution regional model that adequately resolves both the topographic and the baroclinic scales of the motion in the vicinity of a shelf break.

At the northwestern tip of the American continent, Barrow Canyon connects the deep ocean of the Canada Basin with the coastal ocean of the Chukchi shelf. Plate 1 shows the study area. The coastline near Point Barrow changes by almost 90°. In contrast, the shelf break changes its orientation little from 200 km upstream to 200 km downstream of Barrow Canyon. Barrow Canyon is thus oriented perpendicular to the shelfbreak as most canyons are; however, it also parallels the Alaska coast in the Chukchi Sea. The ambient slope current encounters Barrow Canyon the same way as most canyons encounter ambient flows; however, Barrow Canyon is also at the terminus of a strong alongshore shelf flow down the canyon. It is therefore not clear how the canyon models of *Klinck* [1989, 1996], *Allen* [1996], and *Haidvogel and Beckman* [1997] apply to Barrow Canyon. The same applies to observations from "normal" canyons as reported by *Hickey* [1997], *Noble and Butman* [1989], *Freeland and Dorman* [1982], and *Rosenfeld et al.* [1994]. The observations reported in this paper and by *Münchow and Carmack* [1997] indicate that a baroclinic along-canyon flow dominates over Barrow Canyon This flow is an extension of a partly buoyancy driven coastal current that transports fresh Pacific waters through Bering Strait to the Arctic Ocean [*Paquette and Bourke*, 1974; *Aagaard and Roach*, 1990]. Its Pacific waters constitute an ubiquitous water mass that can be traced throughout much of the Arctic Ocean as an anomalous warm and relatively fresh subsurface water [*Coachman and Barnes*, 1961; *Aagaard*, 1984]. These waters are found both in the form of subsurface slope currents [*Aagaard*, 1984] and as submesoscale vortices [*D'Asaro*, 1988a; *Manley and Hunkins*, 1985]. *D'Asaro* [1988b] proposes that the lateral current shear off Barrow, Alaska, and subsequent flow separation generate the vortices that populate much of the Canada Basin. While this scenario explains anticyclonic vortices, it does not explain the also observed cyclonic vortices. Furthermore, even though vortex formation is estimated to occur on a daily timescale, it has yet to be observed directly with modern instrumentation.

Mountain et al. [1976] and *Aagaard and Roach* [1990] analyze data from current meters moored within Barrow Canyon. They measured currents near the bottom and over the flanks of the upper canyon and reported generally downcanyon (northward) bottom currents in excess of 30 cm s^{-1}, temporal variations that correlate well with atmospheric pressure gradients along the coast of Alaska, and occasional upcanyon (southward) surges of warm and salty waters from the Atlantic layer of the Arctic Ocean. Their data, however, do not allow an assessment of either the baroclinicity or the spatial variability of the flow. Such an assessment is the goal of this study.

We investigate the detailed dynamics of the circulation at the intersection between the shallow Chukchi and Beaufort shelves and the deep Arctic Ocean adjacent to the northern coast of Alaska. We use velocity and density observations together with a regional general circulation model to study the interactions of the Alaska Coastal Current [*Paquette and Bourke*, 1974; Münchow and Carmack, submitted manuscript, 1997] with the sloping topography. The study area includes a coastline that changes its orientation by 90° at Point Barrow. Past this point the alongshore coastal current runs almost perpendicular to the strongly sloping bottom topography of the Chukchi and Beaufort shelf break.

In contrast to most studies that report and analyze either observational data or numerical results, we subject both data and numerical results to similar dynamical analyses. The observational data originate from a 1993 survey near the shelf break off northern Alaska. The numerical results originate from a regionally configured general circulation model that we run with very high spatial resolution. In section 2 we describe the observations that motivate the specific choice of the model and its configuration. Section 3.1 discusses the diagnostics of the cross-canyon momentum balance using numerical and observational data. Section 3.2 discusses the strong time dependence of the along-canyon flow. Section 3.3 compares model predictions of the velocity and density fields with those observed. Before we diagnose the along-canyon momentum balance in section 3.4, we explain the observed large temporal variability of the along-canyon velocity field in terms of Kelvin and topographic Rossby wave dynamics. Section 4 summarizes the conclusions of this study.

2. Methodology, Study Area, and Data Sources

We combine analyses of quasi-synoptic acoustic Doppler current profiler (ADCP) and conductivity-temperature-depth (CTD) observations with numerical simulations to analyze the physical mechanisms that affect the flow through Barrow Canyon. A series of sensitivity runs were conducted to formulate forcing and open boundary conditions which are both numerically stable and consistent with the dynamics of the region. Once the model results emulate the observed velocity and density fields, we then use the model output to further analyze the dynamic features and physical processes in Barrow Canyon.

2.1. Observations

In the fall of 1993, the Canadian Coast Guard Ship (CCGS) *Henry Larsen*, an icebreaker, surveyed the Bar-

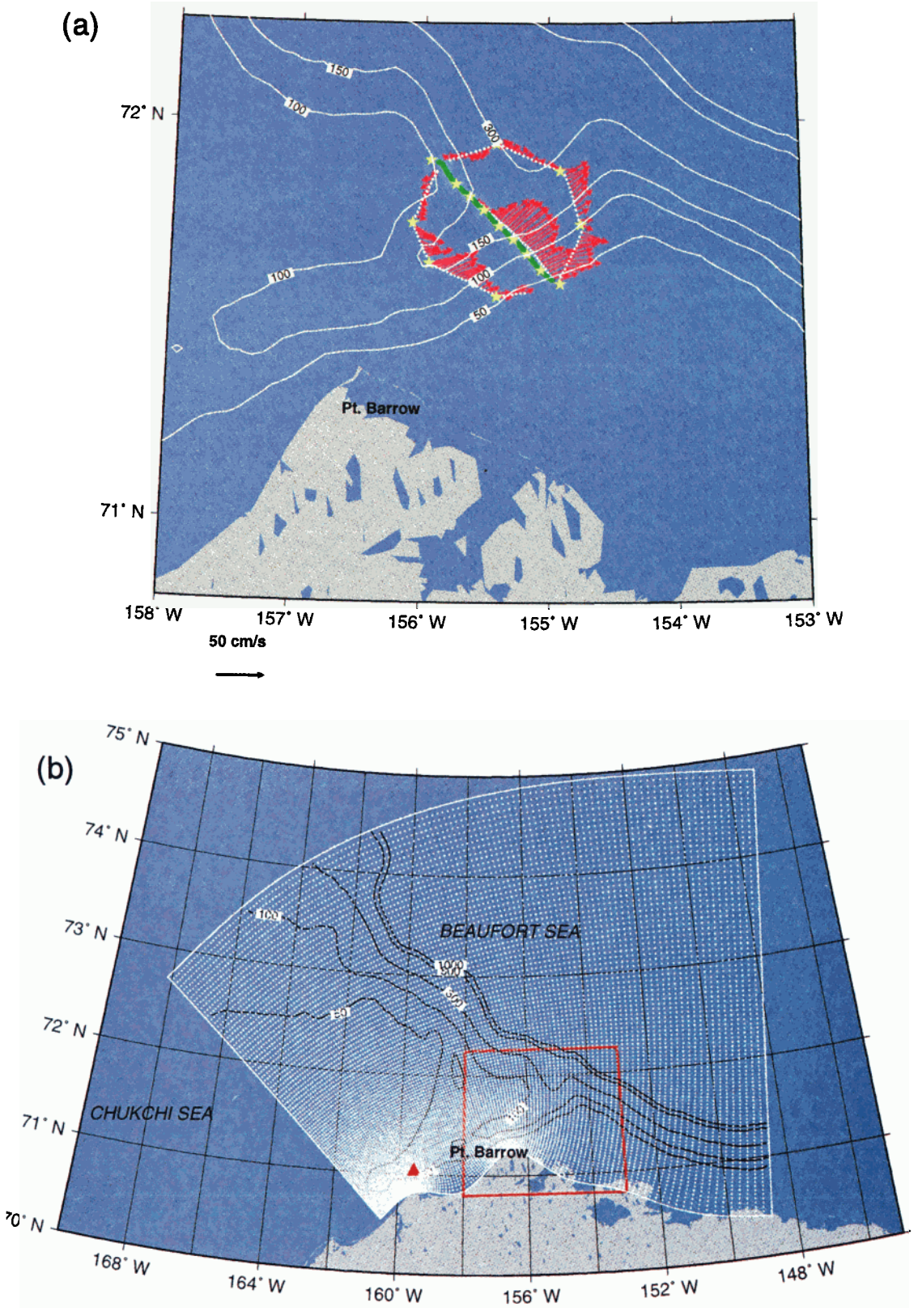

Plate 1. (a) Map of Beaufort Sea showing the ADCP track with superimposed depth-averaged velocity vectors from the September 25, 1993, survey. The yellow stars indicate the location of the CTD casts. The central ADCP transect was conducted twice, once on September 24, 1993 (green diamonds), and once on September 25, 1993 (white dots). (b) Map of the Chukchi and Beaufort Seas showing the model grid and bathymetry (in meters). The grid mesh is shown as white dots. The grid resolution is variable and ranges from about 1.5 km at the lower left corner to nearly 6 km along the eastern edge.

row Canyon and adjacent shelf break regions. The survey included a standard hydrographic component and a nonstandard acoustic Doppler current profiler component. *Münchow et al.* [1995] describe the towed ADCP, as well as its performance and calibration, both off California and Alaska. The ADCP tow system consists of a hydrodynamically shaped tow body that carries a 153-kHz narrowband ADCP. A load conveying, torque balanced, F conductor cable powers the instrument and transmits data back to a shipboard computer. A bungee cord assembly decouples the ship's motion from the ADCP that is towed about 10 m below the surface. We collected data in 8-m vertical bins, 4 pings per ensemble every 10 s, and used a separate bottom-tracking pulse to estimate the ship's speed over ground. During postprocessing, we thoroughly screened these raw data, rejected all velocity profiles for which a bottom-tracking ping was not available, and averaged the screened data into 10-minute averages [*Münchow et al.*, 1995]. This results in a random short-term error of less than 1 cm s^{-1}; however, the thorough calibration reveals bias and directional errors of about 2-3 cm s^{-1}. These errors are of the same magnitude as tidal currrents in the study area [*Mountain et al.*, 1976; *Aagaard and Roach*, 1990]. Therefore we neglect the tidal currents as they are indistinguishable from the noise in the ADCP data. Both the noise and the tidal currents are at least an order of magnitude smaller than the subtidal currents reported here and by *Münchow and Carmack* [1997].

Plate 1a shows a map of the study area containing the details of the data collection. This plate shows the bathymetry of the area (in meters), the ship track (white dots), the location of the CTD casts (yellow stars), the ADCP current vectors (in red) obtained from vertically averaging the ADCP profiles taken on September 25, 1993, and the locations of the ADCP profiles taken along the central transect on September 24, 1993 (green diamonds). Plate 1b shows a larger-scale map of the study area containing portions of the Chukchi and Beaufort Seas. The model domain is shown in white; the red square inset delimits the boundaries of Plate 1a for reference.

In addition to the ADCP data, our analyses include data from a September 1993 current meter record. The mooring location is shown by the red triangle in Plate 1b. The mooring was deployed at a depth of 80 m, 150 km upstream from the location of the ADCP survey; the sensors were placed at approximately 60 m from the surface.

2.2. Modeling

We use a three-dimensional, rigid lid, primitive equation model with orthogonal curvilinear coordinates in the horizontal and a new general coordinate in the vertical (S Coordinate Primitive Equation Model, SPEM5.1). The stretching of this new vertical coordinate (s coordinate) is achieved by using a nonlinear function of z which allows high resolution in the upper ocean while maintaining the bathymetry-following properties of the σ coordinate [*Song and Haidvogel*, 1994]. This particular feature is ideal for the application to Barrow Canyon where both steep topography and strong upper ocean vertical stratification are present.

In the particular case of the rigid lid approach, the z surface coordinate, which is a function of s, consists of two terms:

$$z(s) = h_c s + (h - h_c)C(s), -1 \le s \le 0 \qquad (1)$$

where $C(s)$ is a set of s curves, defined by

$$C(s) = \frac{(1-B)\sinh\theta s/\sinh\theta + B\{\tanh[\theta(s+\frac{1}{2})] - \tanh(\frac{\theta}{2})\}}{2\tanh(\frac{\theta}{2})},$$

In the above formula, θ and B are the surface and bottom control parameters, respectively. Their ranges are $0 \le \theta \le 20$ and $0 \le B \le 1$, respectively. The variable h_c can be the minimum depth of the bathymetry or the width of the surface or bottom boundary layer in which a higher resolution is required. The values $h_c = 20$ m, $\theta = 2.6$, and $B = 0$ were chosen for this study. This choice is the result of a careful analysis and it reflects the best choice of vertical spacing to represent the combined bathymetry and stratification of Barrow Canyon. Thus, with $B = 0$, (1) is reduced to

$$z(s) = h_c s + (h - h_c)\frac{\sinh\theta s}{\sinh\theta} \qquad (2)$$

The model was configured on a high-resolution (1.5 to 5 km) regional grid covering the Beaufort and Chukchi Seas (Plate 1b). The grid is orthogonal and has 12,513 and 25 horizontal and vertical grid points, respectively. The average grid resolution within the CTD domain (yellow stars in Plate 1a) is about 3 km. The 25 vertical grid points can be seen in Plate 4a, which is a cross section of the modeled velocity to be discussed later in section 3.3.

The model was initialized from rest (u=0, v=0). The initial temperature (T) and salinity (S) fields were specified by choosing analytical expressions which emulate the observed vertical stratification (based on the 1993 CTD observations). The analytical expressions for the initial T and S fields are provided in Table 1. Note that T and S are only a function of depth (z). Therefore the initial horizontal density gradient is zero. As the 1993 CTD observations did not go below 300 m, the analytical expressions for T and S were designed to asymptotically reach climatological values. These climatological values are $T = 0^o$ C and $S = 34.5$ practical salinity units (psu), which are within the range of the area-averaged Levitus data [*Levitus et al.*, 1994a; *Levitus et al.*, 1994b] for the Arctic at those depths [*Hedström et al.*, 1995]. The equation of state is nonlinear (D. R. Jackett and T. J. McDougall, Stabilization of hy-

Table 1. Analytical Specification of the Initial Temperature and Salinity Fields for the Numerical Experiment

Depth Range			Temperature, °C	Salinity, psu
	z	< 30 m	2	30.5
30 m ≤	z	< 70 m	2 - 3(z-30)/40	30.5 + 2(z-30)/40
70 m ≤	z	< 100 m	-1	32.5
100 m ≤	z	< 130 m	-1 + (z-100)/30	32.5 + 2(z-100)30
	z	> 130 m	0	34.5

drographic data, submitted to *Journal of Atmospheric and Oceanic Technology*, 1994) and uses the potential temperature to calculate the in situ density.

The grid has open boundaries at the southwest, north, and east sides of the domain which must be specified. The model is forced at the southwest boundary by a 40-km-wide barotropic jet representing the mean Bering Strait transport of 1 Sv. At this boundary, the along-canyon velocity, u, is specified, the cross-canyon velocity, v, is set to zero, and constant vertical stratification is imposed. In the interior, the density is initially stratified using the linear expressions of Table 1, as in the open boundary, but it is allowed to evolve temporally and spatially under the influence of advection and mixing.

The current meter data (Figure 4) and the two consecutive ADCP surveys show that there is significant temporal variability in the flow within Barrow Canyon. Since this flow originates in the Bering Strait, one concludes that this variability is due to temporal changes in the Bering Strait northward transport that propagate downstream to Barrow Canyon. *Coachman and Aagaard* [1988] show that the Bering Strait transport variability is highly correlated with the local component of the wind along the axis of the strait. This process is the primary cause for the observed transport variability in Barrow Canyon. In this study we focus our numerical experiment on the traansport changes observed during the September 24-25 ADCP survey, which showed a change from about 0.5 to 1.1 Sv within approximately 16 hours. Therefore, the jet is modulated sinusoidally with a period of 1.5 days and an amplitude of 0.5 Sv in order to emulate the time dependency observed in the data.

The Beaufort Undercurrent was included in our model experiment via an open boundary parameterization of the stream function at the northern limit of the model domain. Since the undercurrent transport along the shelf break is expected to be very small and bathymetrically steered, an upper limit was established by using the simplified expression for the maximum entropy equilibrium solution of *Eby and Holloway* [1994] as

$$\psi = -fL^2H \tag{3}$$

where ψ is the stream function, f is the Coriolis parameter, L is the eddy length scale, and H is the total depth. The value of L is adjustable and dependent on the latitude. *Eby and Holloway* [1994] propose a formula in which L diminishes from 15 km near the equator to 3 km near the pole. Therefore we chose $L = 3$ km for our study.

At the east open boundary the normal gradient of ψ is set to zero and a sponge layer is applied to the outermost 10 grid cells. The baroclinic part of the velocity field at this downstream boundary is obtained by specifying values identical to those just inside the boundary. We conducted numerous test runs before the final choice of eddy viscosities for the model were made. The horizontal viscosity and diffusivity are Laplacian with constant values. Value ranges of 50-500 and 25-100 $m^2\ s^{-1}$, respectively, were tested. The criterion for the optimum choice of horizontal eddy viscosity and diffusivity was based on obtaining the minimum values that provided stable numerical results and the least numerical noise. These values were 100 and 50 $m^2\ s^{-1}$, respectively. There are several choices in SPEM to formulate vertical eddy viscosity and diffusivity. We initially tried the more sophisticated formulations available, such as the Mellor-Yamada turbulence closure scheme and the Richardson-number-dependent formulation of Pacanowsky and Philander. Then we compared the results of the two above schemes with the results from other runs using constant vertical eddy viscosity and diffusivity (with ranges of 0.0005-0.005 $m^2\ s^{-1}$ and 0.00005-0.0005 $m^2\ s^{-1}$, respectively). The model run that produced best results, e.g., agreement with the observed velocity and density fields and minimum amount of numerical noise, was the run with constant values of vertical viscosity and diffusivity. The best values of vertical viscosity and diffusivity, according to the above criterion, were 0.001 and 0.0001 $m^2\ s^{-1}$, respectively.

Numerous model runs, ranging in duration from 5 to 20 days, were conducted to test model response to boundary conditions and verification with the available data. The final run had a duration of 20 days. The possible influence that the Beaufort Gyre may have on our study area was not analyzed in this study because its inclusion would require a much larger scale modeling effort (quite possibly the entire Arctic Ocean) which goes beyond the scope of the present study. According to *Aagaard* [1984], the Beaufort Undercurrent typically extends from the near surface to the bottom between the

50- and 2500-m isobaths; a distance of 60-70 km. Therefore the Beaufort Undercurrent constitutes the primary dynamic interaction with the flow in Barrow Canyon. The Beaufort Gyre lies further offshore and therefore its influence is significantly reduced.

3. Analysis and Discussion

Initial scaling arguments helped the choice of the modeling strategy and data analysis. The Rossby (R= U/fL) and Froude (Fr=U/NH) numbers are R=0.1 and Fr=0.4, respectively. The parameters to calculate R and Fr are L=40 km (width of the canyon), H=50 m (typical vertical scale), f=1.4 x 10^{-4} , N^2=-$[g/\rho_0]$ $(\partial\rho/\partial z)$=7 x 10^{-4}, and U= 0.5 m s^{-1}. The small Rossby number and the Froude number less than 1 indicate that both stratification and rotation are dynamically important.

We combine the observations from September 1993 with the results of the numerical simulation to evaluate the cross-canyon (y) and along-canyon (x) momentum balances. We estimate the ageostrophic contributions to determine their significance in the momentum balance. *Dewey et al.* [1991] point out that a high correlation between the Coriolis acceleration and the pressure gradient term is not sufficient in determining the degree of geostrophy. Ageostrophic contributions are often omitted from geostrophic diagnosis because they are difficult to measure, require repeated observations, and thus are assumed to be small. To determine the degree of geostrophy, each term in the momentum equations should be estimated. Only when it has been established that the ageostrophic terms are in fact insignificant can it be stated that the flow is geostrophic. Our unique data set, combined with results of the model simulation, allows a complete assessment of the relative importance of momentum terms.

Plate 2a shows the density along the central transect with superimposed contours of the observed velocity from the September 24 survey. Plate 2b shows the observed velocity field along the same central transect from the September 25 survey (16 hours later). The density field is not shown because there were no CTD casts taken during this second survey. Note the significant increase in flow intensity between the two surveys (downcanyon transport doubles), which is mostly due to an increase of the barotropic component. We will compare these observed fields with the corresponding model fields in section 3.3.

3.1. Cross-Canyon Momentum Balance

We evaluate the cross-canyon momentum balance using data from the central ADCP transect. Since this central transect was surveyed twice within 16 hours, the time derivative ($\partial v/\partial t$) can also be evaluated. The cross-canyon momentum equation is

$$\frac{\partial v}{\partial t} + u\frac{\partial v}{\partial x} + v\frac{\partial v}{\partial y} =$$

$$-fu - \frac{g}{\rho_0}\frac{\partial}{\partial y}\int \rho dz - g\frac{\partial \eta}{\partial y} + D_v \qquad (4)$$

where u is the along-canyon velocity, v is the cross-canyon velocity, and ρ is the density. The first term on the left-hand side of (4) is the time derivative of the cross-canyon component of the velocity, the second and third terms are the advective (nonlinear) terms. The first term on the right-hand side of (4) is the Coriolis acceleration, the second term is the baroclinic pressure gradient, the third term is the barotropic pressure gradient, and the last term (i.e., D_v) represents the horizontal and vertical eddy viscosity terms. Since the barotropic component of the pressure gradient ($-g\partial\eta/\partial y$) cannot be directly evaluated, it becomes an implicit component of the residuals in the following momentum balance:

$$\frac{\partial v}{\partial t} + u\frac{\partial v}{\partial x} + v\frac{\partial v}{\partial y} + fu + \frac{g}{\rho_0}\frac{\partial}{\partial y}\int \rho dz = \qquad (5)$$

$$-g\frac{\partial \eta}{\partial y} + residuals$$

Figures 1a through 1e show the magnitude of each component relevant to the cross-canyon momentum balance shown in (5). The units for the momentum terms are 10^{-3} cm s^2.

The large magnitude and vertical uniformity of the residuals (Figure 1e) suggest that the cross-canyon barotropic pressure gradient plays a major role in the dynamic balance. This holds for both upcanyon and downcanyon flows that occur at different locations concurrently.

We simplify the analysis of the momentum balance by reducing the information provided in Figures 1a through 1e to cross-canyon averaged values for four different vertical layers. The result is shown in Table 2. Note the importance of the barotropic pressure gradient shown by the small vertical variability of the residuals in the last column of Table 2. Despite the relatively smaller size of the ageostrophic terms (i.e., $\partial v/\partial t$ and $u\partial v/\partial x + v\partial v/\partial y$), they may contribute significantly to the momentum balance and further analysis of their contribution is appropriate.

To make the momentum analysis more clear, we separate the barotropic component of the balance from the baroclinic component by vertically averaging the individual components of the momentum terms shown in the last row of Table 2. These averages therefore represent the barotropic component of the momentum balance across the canyon. Geostrophy can be immediately inferred from the relative magnitude of these barotropic terms. The Coriolis acceleration and the pressure gra-

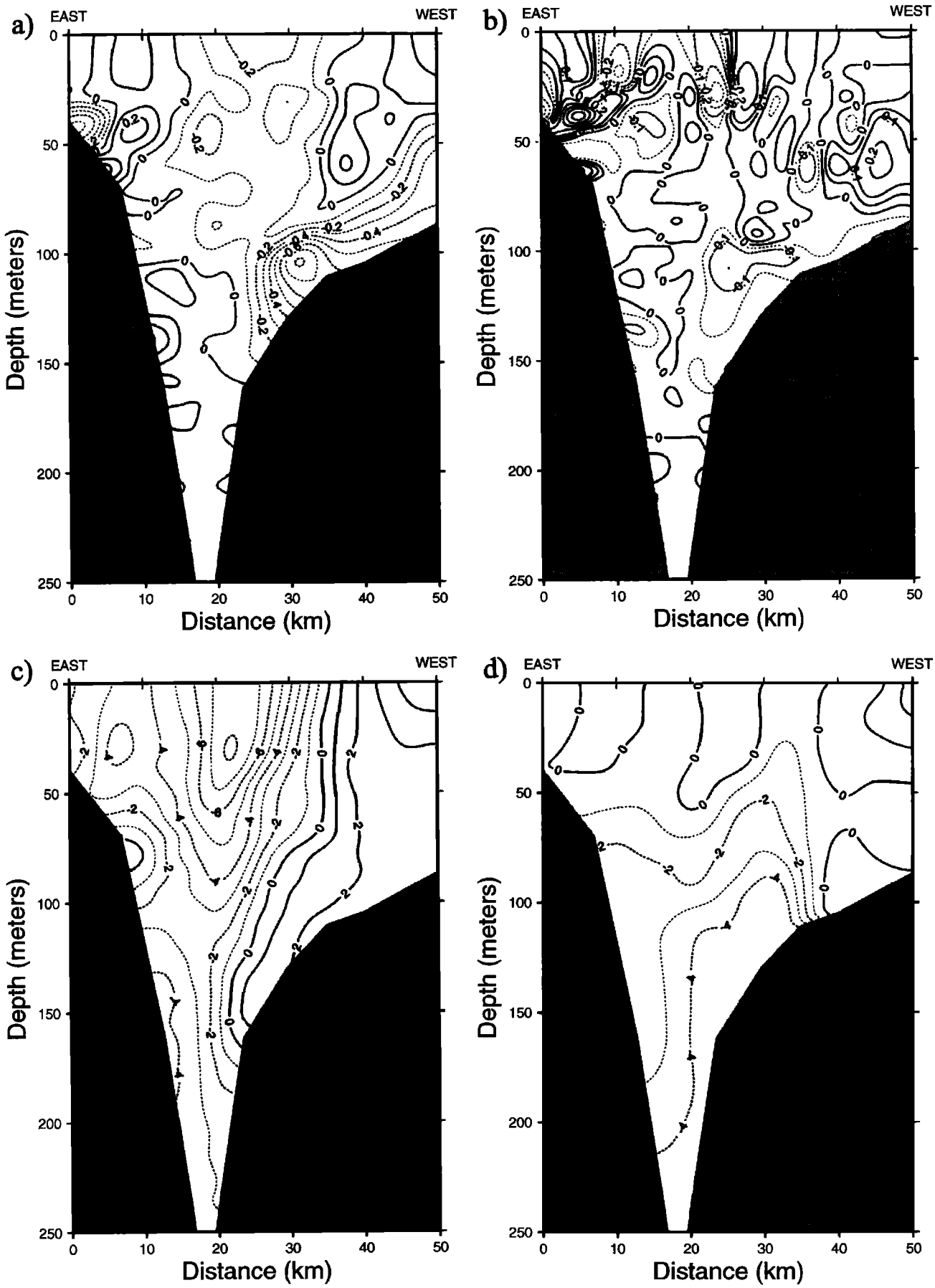

Figure 1. (a) Cross-canyon velocity time derivative, (b) advective terms, (c) downcanyon Coriolis acceleration, (d) crosscanyon baroclinic pressure gradient, and (e) momentum balance residuals at the central transect. All units are in 10^{-3} cm s^{-2}.

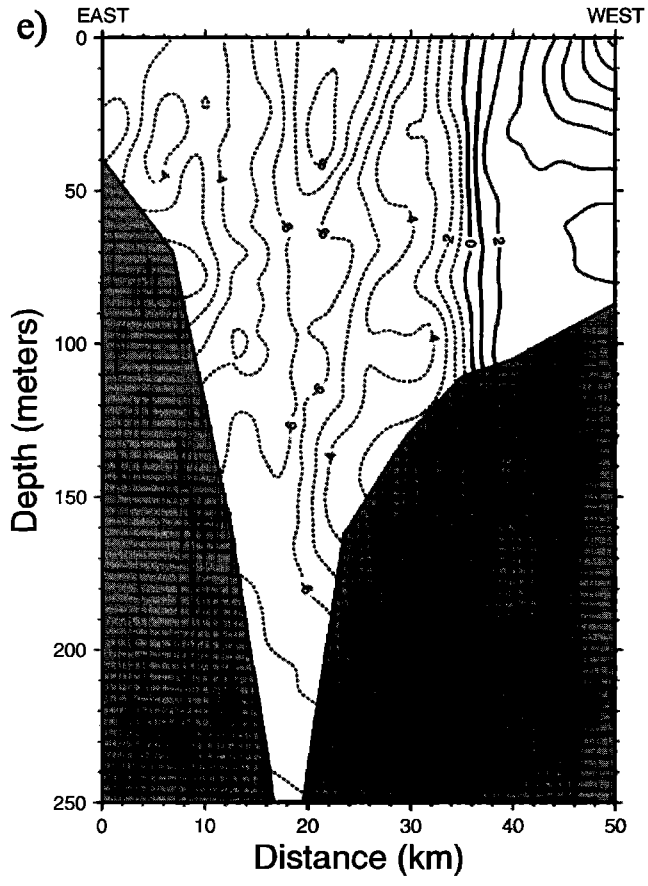

Figure 1. (Continued)

dient terms are significantly larger (at least 1 order of magnitude) than the ageostrophic terms.

To obtain the baroclinic momentum balance we subtract the vertically averaged values from the values of each layer in Table 2. The result is shown in Table 3. We can readily see that the momentum balance of the baroclinic component is ageostrophic since the residuals, the time derivative, and the nonlinear terms are not negligible when compared with the Coriolis acceleration and baroclinic pressure gradient. The ageostrophic terms, including the residuals which implicitly contain the vertical viscosity term (i.e., $A_v \partial^2 v'/\partial z^2$), are all a function of v', the cross-canyon velocity component. The velocity component v' is the secondary flow, which is the flow in the plane normal to the direction of the main axis of the canyon. The secondary flow results from a local imbalance between the vertically varying Coriolis acceleration (fu') and the cross-canyon pressure gradient. From Table 3 we notice that this imbalance changes sign at approximately middepth, indicating a reversal of the secondary flow.

Secondary circulation generated by this mechanism has been investigated based on observations, analytical treatment, and laboratory experiments [*Geyer*, 1993; *Johnson and Sanford*, 1992; *Johnson and Ohlsen* 1994]. The strength of the secondary flow varies from 5 to 15% of the streamwise flow [*Geyer*, 1993]. Therefore, since the along-canyon velocity is of the order of 100 cm s^{-1}, the strength of the secondary flow should be between 5 and 15 cm s^{-1}.

Figure 2 shows vertical profiles of the along-canyon (u) and cross-canyon velocity (v) components from a single ADCP profile taken in the middle of the canyon on September 25. The u component has a strong vertical shear which accounts for the forcing of the secondary flow via the Coriolis term fu'. The v component of the velocity is the secondary flow which has a maximum strength of about 8 cm s^{-1}; the flow is northwestward above 120 m and southeastward below 120 m.

In summary, the momentum balance across the canyon is geostrophic only for the barotropic component of the flow. The baroclinic component of the cross-canyon momentum balance is ageostrophic. Furthermore, the resulting imbalances from geostrophy generate a secondary flow with strength proportional to the vertical shear of the along-canyon flow. Although the secondary flow is small when compared with the strength of the along-canyon flow, it has significant influence on the dynamics and kinematics of the canyon regime. The transverse exchange accomplished by the secondary flow influences the structure of the along-canyon flow by changing the horizontal and vertical distributions of momentum.

3.2. Temporal Variability of the Along-Canyon Flow

Even though the barotropic along-canyon flow appears to be in geostrophic balance (Table 2), the ADCP data suggests a strong time dependence of this flow. On

Table 2. Cross-Canyon Momentum Terms Averaged Across the Width of the Canyon

Depth Range	$\frac{\partial v}{\partial t}$	$(u\frac{\partial v}{\partial x}+v\frac{\partial v}{\partial y})$	fu	$\frac{1}{\rho_o}\frac{\partial p}{\partial y}$	Residual
10-30 m	0.	0.	-2.30	.21	2.09
30-70 m	-0.05	-0.02	-1.71	-0.53	2.27
70-100 m	-0.17	-0.01	-0.23	-1.62	2.04
100-155 m	-0.26	-0.04	-0.04	-2.57	2.91
Vertical Average	-0.11	0.	-1.15	-1.04	2.30

Values are given in 10^{-3} cm s^{-2}. The average was computed using data from the central ADCP transect.

Table 3. Cross-Canyon Baroclinic Momentum Terms Averaged Across the Width of the Canyon

Depth Range	$\frac{\partial v'}{\partial t}$	$(u'\frac{\partial v'}{\partial x}+v'\frac{\partial v'}{\partial y})$	fu'	$\frac{1}{\rho_o}\frac{\partial p'}{\partial y}$	Residual
10-30 m	0.11	-0.	-1.15	1.24	-0.20
30-70 m	0.06	0.03	-0.56	0.50	0.03
70-100 m	-0.06	0.	0.92	-0.59	0.27
100-155 m	-0.15	-0.04	1.12	-1.54	-0.61

Values are given in 10^{-3} cm s^{-2}. The values tabulated were obtained by subtracting the vertically averaged values shown in Table 2.

September 24/25, 1993, the total along-canyon volume transport changed from 0.5 ± 0.1 Sv to 1.1 ± 0.1 Sv within about 16 hours [*Münchow and Carmack*,1997]. In Figure 3 we compare the observed and simulated depth-averaged time derivative ($\partial\bar{u}/\partial t$). It indicates flow accelerations that change sign near the center of the canyon; that is, the upcanyon flow on the western side of the canyon increases concurrently with the downcanyon flow on the eastern side of the canyon next to the coast.

The maximum value of the observed time derivative is about 0.6 (in 10^{-3} cm s^{-2}). A 3 cm s^{-1} velocity error Δu results in an error in the local acceleration $\Delta(\partial u/\partial t)$ of about 0.1 x 10^{-3} cm s^{-2} due to $\Delta(\partial u/\partial t) \simeq 2\Delta u/T$. The error bar resulting from this analysis is shown in Figure 3.

The Coriolis term in the along-canyon momentum balance, fv, ranges from 0.5 to 1 in the same units, since f is of the order of 10^{-4} s^{-1} and typical values of v range from 5 to 10 cm s^{-1}. The ratio of the along-canyon velocity time derivative to the Coriolis acceleration ($R_t = [\partial u/\partial t]/fv$), i.e., the temporal Rossby number, is of the order of 1. Consequently, the along-canyon momentum balance is ageostrophic.

The simulated time derivative exhibits a less sharp sign transition than the observed time derivative, which indicates that the observed horizontal velocity shear is much stronger than the simulated shear. We attribute this discrepancy to insufficient horizontal grid resolution at that location (order of 4 km).

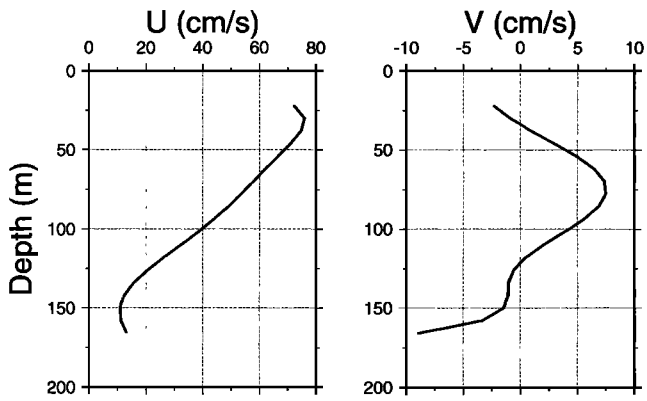

Figure 2. Vertical profiles of along-canyon (u) and cross-canyon (v) horizontal velocity components.

Figure 4 shows a September 1993 composite time series of wind vectors (meters per second) at Point Barrow and data from a current meter moored 150 km upstream from our study area. The two dashed vertical bars show the approximate time of the two ADCP cross-canyon transects. This month-long record emphasizes the strong temporal variability of the along-canyon flow. Note the three upcanyon current reversals, in particular, the September 20-21 reversal, which was accompanied by an intrusion of colder and saltier water into the canyon. This particular reversal took place a few days prior to the ADCP survey.

3.3. Comparison Between Model Results and Observations

Next, we conduct a comparison between the simulated and observed fields in order to demonstrate that the model provides realistic enough results to be able to use them in our dynamic analysis. In Figure 5 we com-

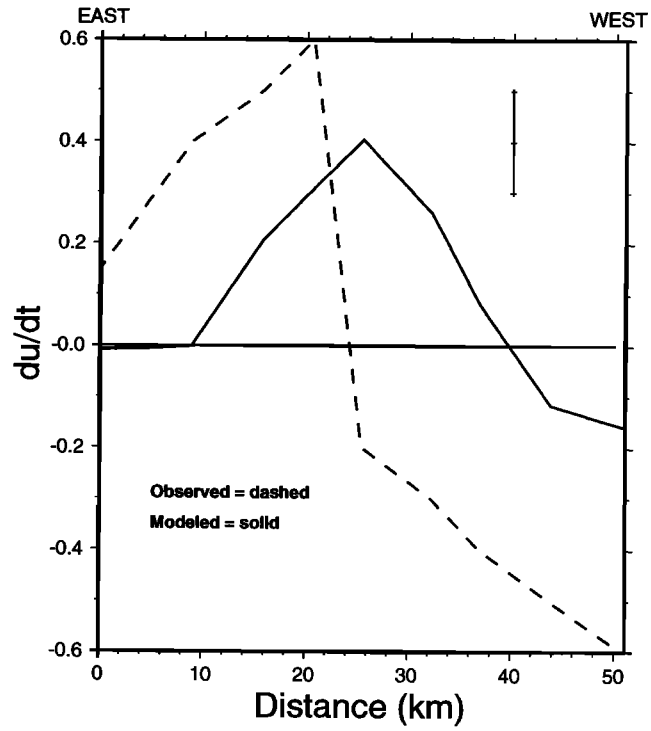

Figure 3. Comparison between observed and simulated depth-averaged velocity time derivatives.

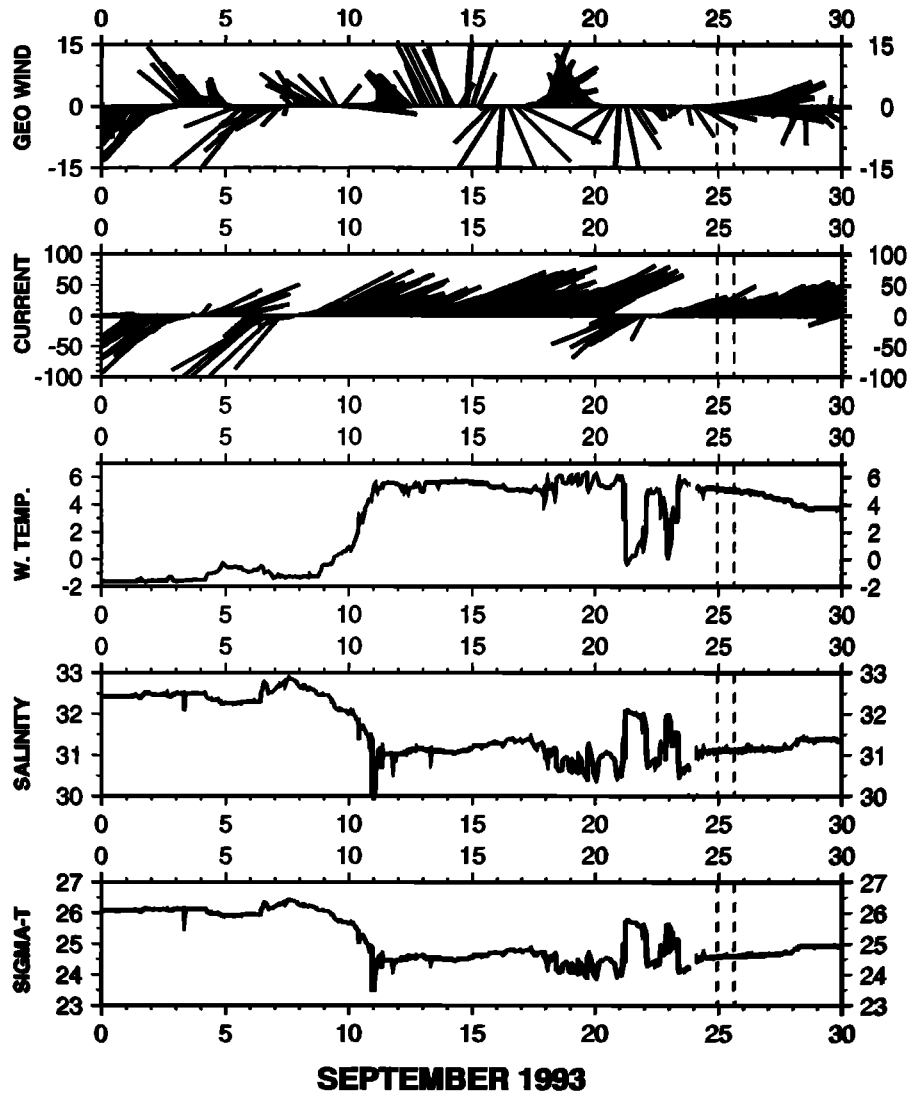

Figure 4. Composite time series of wind vectors (in meters per second) at Point Barrow, velocity (in centimeters per second), temperature (in degrees Celsius), salinity (in practical salinity units), and density (in kilograms per cubic meter) from a current meter deployed at a site located 150 km upstream from the ADCP survey site where the depth is 80 m (observation depth is 60 m). Note the three upcanyon current reversals, in particular, the September 20-21 reversal which was accompanied by an intrusion of colder and saltier water into the canyon. The two vertical dashed lines indicate the times of the two ADCP transects. The data were provided by Tom Weingartner, University of Alaska Fairbanks (UAF).

pare the simulated stream function (dashed lines) with the calculated depth-averaged stream function from the ADCP data (solid lines). The inset in Figure 5 contains a time series (in days) of the transport (in Sv) imposed at the southwest open boundary; it indicates the time (black circle) at which the stream function snapshot was taken from the model output. At this time, the simulated downcanyon transport (1.6 Sv) agrees with the observed transport of September 25. The observed stream function field is confined to a much smaller area since the velocity survey covers only a small portion of the spatial domain.

The simulated stream function field depicts some interesting features of the regional flow. The total transport from southwest to northeast is 2 Sv, with about half of the flow (1 Sv) flowing parallel to the isobaths along the coast. The remaining 1 Sv originates from farther offshore. The flow crosses isobaths and is entrained into the canyon where it joins the Beaufort Undercurrent along the shelf break downstream. Seaward of the 100-m isobath, near the mouth of the canyon, the Beaufort Undercurrent meanders in and out of the canyon, in close agreement with the pattern shown by the observed stream function field.

To better illustrate the time dependency of the along-canyon flow, we now discuss two snapshots of the velocity and density fields as they are predicted by the model. Plate 3 shows velocity vectors at a depth of 30 m about

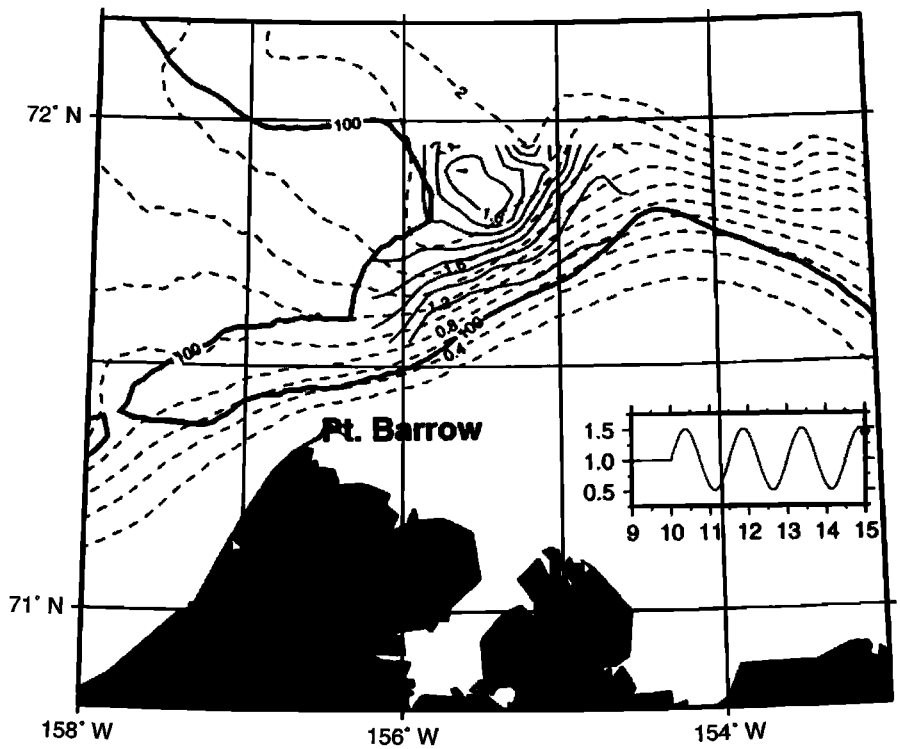

Figure 5. Stream function map from observed (solid lines) and simulated (dashed lines) velocity fields. At this time (15 days after model start), the magnitude of the downcanyon transport generated by the model approaches that of the September 25 ADCP survey. The inset shows a time series of the sinusoidal transport at the western boundary of the model; the black dot represents the time of the stream function snapshot.

14 days after model start. At this time, the magnitude of the downcanyon velocity field approaches that of the September 24 ADCP survey when the along-canyon volume transport reached 0.5 Sv. Note the presence of the small 20-km-wide cyclonic recirculation on the western side of the canyon. The line of green diamonds indicates the location of the ADCP transect where we next compare the model derived cross-canyon velocity and density fields (Plates 4a and 4b) with the corresponding observed fields (Plate 2). The model generates velocity and density fields with sloping isopycnals which agree well with the observed fields. Note the two pycnoclines: a shallow pycnocline between depths of 30 and 70 m (light blue to dark green) and a deeper pycnocline between depths of 100 and 120 m (light green to yellow). The deep pycnocline corresponds to the main halocline of the Arctic Ocean that is raised more than 100 m into Barrow Canyon. Note the pinching of the isopycnals in the deep pycnocline on the east (left) side of the canyon and the spreading on the west side, giving the density field a wedge shape. This pattern, which is shown by both observed and modeled density fields, agrees with results of previous investigations on the effects of secondary flows on density stratification. *Johnson and Ohlsen* [1994], in a laboratory experiment of two-layer exchange through channels, showed that the interface was sharpened on its deep side and spread on its shallow side by the strain field of the secondary circulations. In the presence of mixing, this strain field causes a wedge-shaped density field within the channel. A similar pattern has been observed in outflows through the Vema and Faroe Bank channels [*Johnson and Sanford,* 1992].

Plate 5 shows velocity vectors at a depth of 30 m, about 15 days after model start. At this time, the magnitude of the downcanyon velocity field approaches that of the September 25 ADCP survey when the along-canyon volume transport reached 1.1 Sv. Note again the presence of a 20-km-wide cyclonic recirculation feature on the western side of the canyon (upper left corner of Plate 5). It represents the entrainment of Chukchi shelf water into the canyon from depths less than 100 m.

Plates 6a and 6b show the predicted velocity and density fields along the section shown in Plate 5. We believe that these two snapshots adequately represent the spatial (Plate 1) and temporal (Figures 3 and 4) variability of the data. A comparison between Plates 2, 4 and 5 shows that both data and model flow intensification, most noticeable below 50 m, is from 10 cm s^{-1} to greater than 50 cm s^{-1}. In addition, both data and model results show a significant decrease of the vertical shear in the deepest part of the canyon; this indicates that the sudden incease (50%) of downcanyon trans-

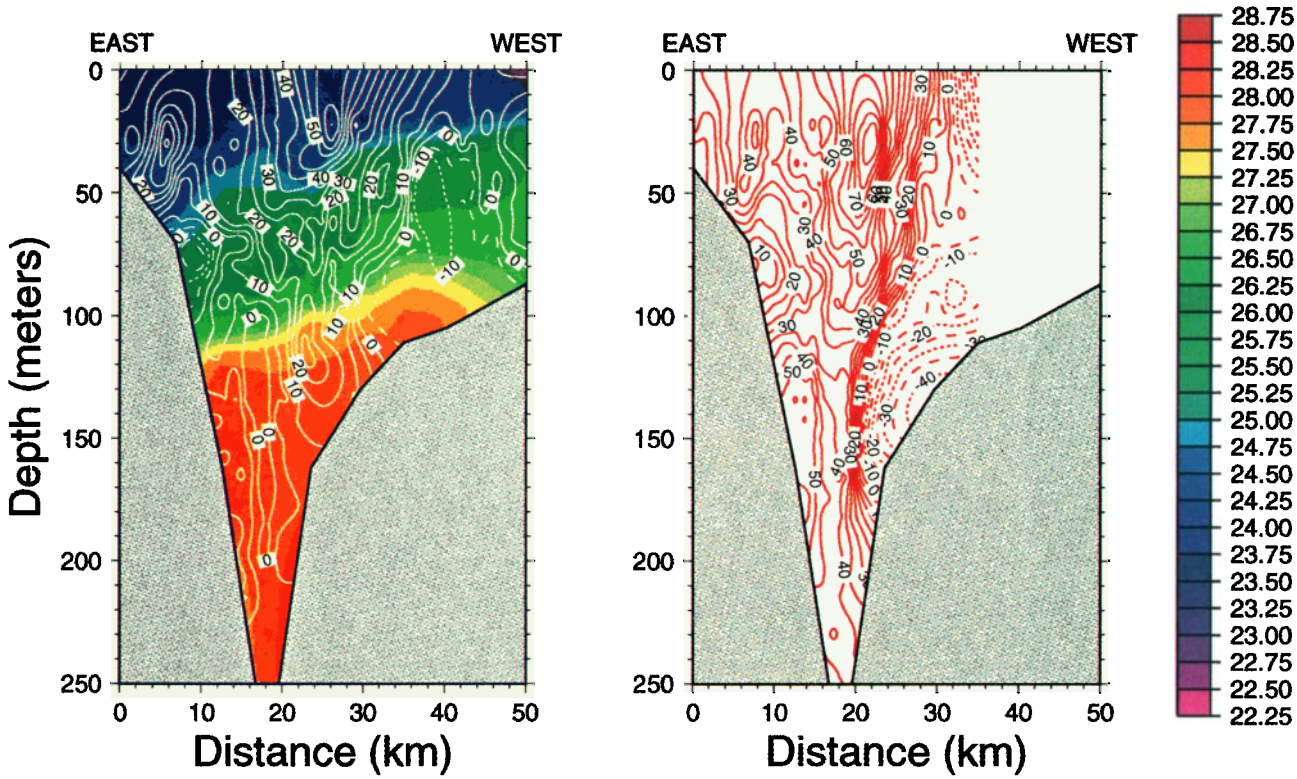

Plate 2. Observed cross-canyon section of velocity and density. (a) Velocity and density cross sections from the September 24, 1993, ADCP and CTD transects. (b) Velocity cross section from the September 25, 1993, ADCP transect (CTD transect not available). Note in plate 2a the two pycnoclines: a shallow pycnocline between depths of 30 and 70 m (light blue to dark green) and a deeper pycnocline between depths of 100 and 120 m (light green to yellow). The deep pycnocline corresponds to the main halocline of the Arctic Ocean that is raised by more than 100 m into Barrow Canyon.

port is primarily achieved by an intensification of the barotropic component of the flow. The maximum observed and modeled surface velocities are quite similar (data, 55-80 cm s^{-1}; model, 65-75 cm s^{-1}). However, the core near-surface maximum velocity in the data is mainly centered along the axis of the canyon, while the model results show the core of maximum near-surface velocities placed at the eastern flank of the canyon. One possible explanation for this is the absence of the Beaufort Gyre in the numerical simulations. The westward flowing Beaufort Gyre opposes the shelf break eastward flow that originates from Barrow Canyon. Dynamical interactions between these two currents may have an effect on the horizontal shear intensity and the placement of the downcanyon jet. For instance, at a depth of 150 m, the highest horizontal shear shown by the data is about 18 cm s^{-1} km^{-1}, while the model's highest horizontal shear at that same depth is about 9 cm s^{-1} km^{-1}, or 50% less than the observed horizontal shear. However, to include the effects of the Beaufort Gyre in our simulations would require a much more ambitious numerical study that includes the whole Arctic Ocean with basin-scale forcing of gyre-scale duration (3 to 5 years). This effort is beyond the scope of the present study.

Even though the inclusion of the Beaufort Gyre in our simulations could have made our results more realistic, the model reproduces the barotropic component well and thus agrees with the results of our momentum balance analysis discussed in the previous section. Therefore we feel justified to use the model results to diagnose the along-canyon momentum balance over Barrow Canyon.

3.4. Along-Canyon Dynamics

Before we diagnose the along-canyon momentum balance, we will first diagnose how temporal perturbations in the upstream inflow propagate down the canyon. Figure 6a shows a plot of the time of arrival (Δt) of the maximum transport perturbation at six different locations along the axis of the coastal jet (Figure 6b). The vertical coordinate shows the distance traveled (Δx) from the southwest open boundary (forcing). The tangent of the curve in Figure 6a, $\Delta x/\Delta t$, is the phase speed of the transport disturbance. There is a noticeable change to a faster phase speed at a distance of 100 km from the southwest boundary. Up to the distance of 100 km, the phase velocity is 13 m s^{-1}. For distances greater than 100 km the phase velocity doubles to val-

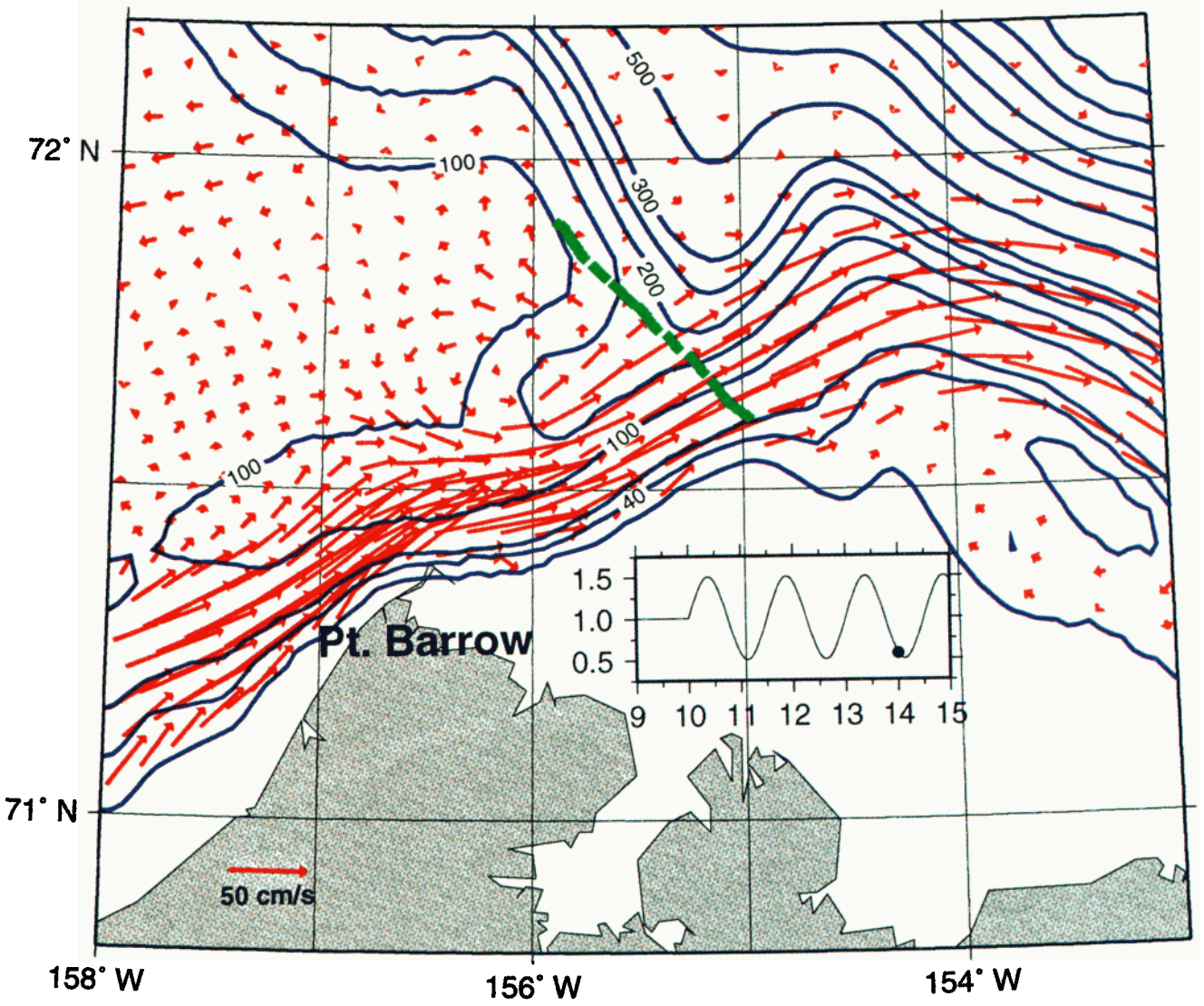

Plate 3. Snapshot (14 days after start) of model-generated velocity vectors at a depth of 30 m. For clarity, the map shows model vectors from a subset of grid points (every other point) surrounding the ADCP survey area. Note the small eddy (radius of about 10 km) on the western side of the canyon. At this time, the magnitude of the downcanyon velocity field generated by the model approaches that of the September 24 ADCP survey. The line of green diamonds indicates the location of the CTD transect; grid points at or closest to these points were used to produce the model derived velocity and density transects shown in Plate 4.

ues ranging from 23 to 27 m s^{-1}. The phase velocity of a barotropic gravity wave ($\sqrt{gH}$) ranges from 22 to 26 m s^{-1} corresponding to depths of 47 and 71 m, respectively. The phase velocity inferred from the model for distances greater than 100 km agrees well with the gravity wave phase velocity. The model-derived phase velocity (10-13 m s^{-1}) for distances less than 100 km, however, is too slow for Kelvin or Poincaré waves and too fast for purely advective translation. We explain this apparent discrepancy with the sharp change of across-shore bottom slope. The average bottom slope (α_0) is about 4 x 10^{-4} up to a distance of 100 km downstream from the forcing boundary. Then it increases rapidly beyond that distance and reaches α_0 = 12 x 10^{-4} at a distance of 200 km downstream. The trifold increase of the across-shore bottom slope is conducive to a transition of propagation regime. For the gentler bottom slopes, such as the wide shelf area of the domain (Chukchi Sea), we will demonstrate that the disturbances propagate as a topographic wave, while for the steeper slopes further downstream the disturbances travel as Kelvin waves. This assertion is supported by comparing our phase velocity of 13 m s^{-1} with the phase velocity of a topographic wave traveling in the x direction, i.e., along isobaths.

The frequency and phase velocity of a topographic wave [*Cushman-Roisin*, 1994] are given by $\omega = \alpha_0 gk/f(1 + R^2k^2)$ and $C_x = \alpha_0 g/f(1 + R^2k^2)$, respectively,

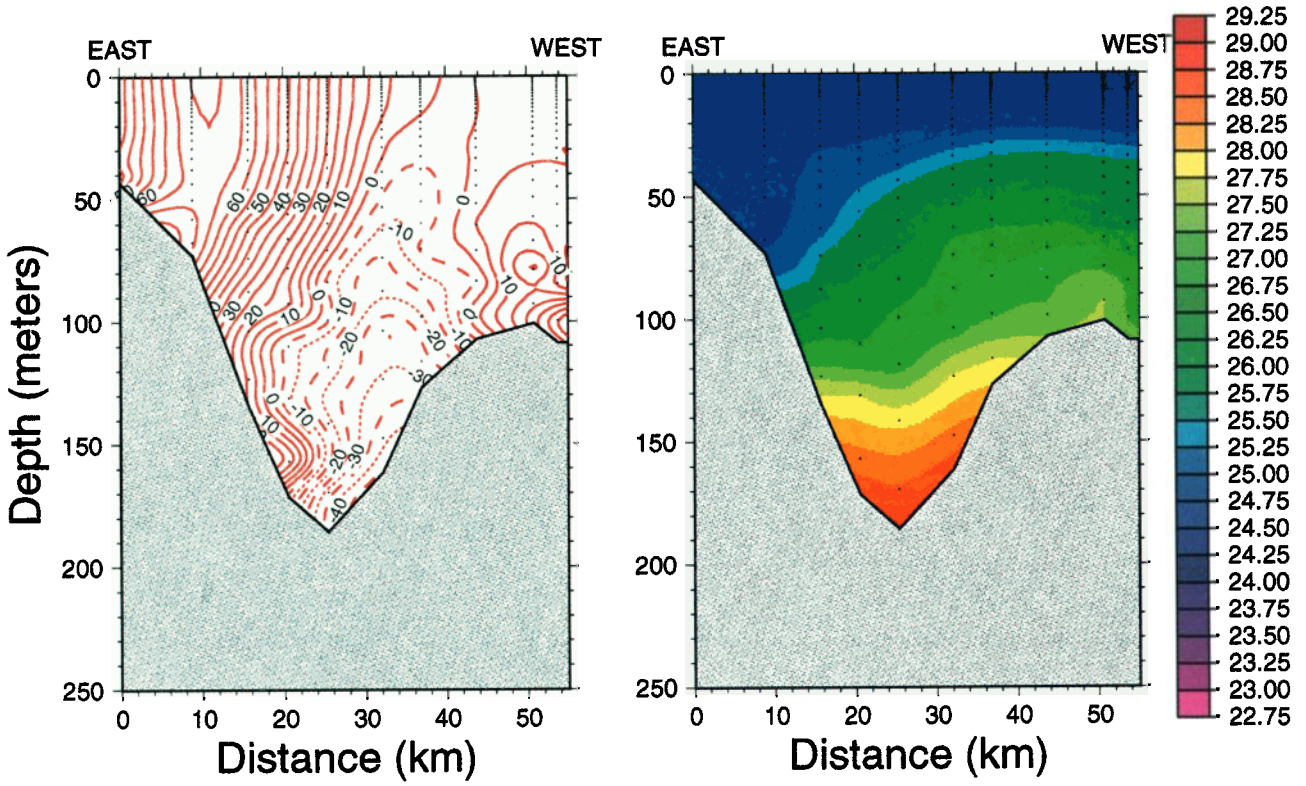

Plate 4. Model-generated (left) velocity and (right) density transects at 14 days after start. The black dots represent the location of the vertical grid points in the model.

where α_0 is the bottom slope, g is the acceleration due to gravity, f (1.4 x 10^{-4}) is the Coriolis factor, $R = \sqrt{gH_0}/f$ (150 km) is the Rossby radius of deformation, and k is the wave number. The bottom slope is required to be gentle ($\alpha_0 = 4 \times 10^{-4}$) so that the ratio of the change in water depth experienced by a water parcel during passage of a wave to the water depth is small ($\ll$ 1). Another constraint is that there exists a maximum frequency, $\mid \omega \mid_{max} = \mid \alpha_0 g \mid / \mid 2fR \mid$, above which topographic waves cannot be generated. This constraint is also satisfied since $\mid \omega \mid_{max} = 9.3 \times 10^{-5}$ s^{-1} and the forcing frequency is 4.9 x 10^{-5} s^{-1} (period of 1.5 days). Therefore, topographic waves can be generated on the Chukchi Sea shelf and, within the gentle slope portion of the model domain, have a speed given by C_x. At a distance of 200 km downstream where the slope $\alpha_0 = 12 \times 10^{-4}$, $\mid \omega \mid_{max} = 2.8 \times 10^{-4}$ s^{-1}, which is larger than f ($\mid \omega \mid_{max} = 2f$). This violates the condition of subinertial motions and is thus meaningless. The wave theory, however, applies to waves at that region whose frequencies are much less than the maximum value. Therefore topographic waves are supported in the two regions.

To calculate the phase speed at the forcing frequency of 4.9 x 10^{-5} s^{-1}, we must first calculate the corresponding wave numbers from $\omega = \alpha_0 gk/f(1 + R^2k^2)$. This equation is quadratic in k and for $\alpha_0 = 4 \times 10^{-4}$ yields two wave numbers, 0.2 x 10^{-5} m^{-1} and 2.4 x 10^{-5} m^{-1}. These wave numbers correspond to wave speeds 26 and 2 m s^{-1}, respectively. So, at the forcing frequency, the topographic wave speeds are too fast or too slow when compared to the 13 m s^{-1} given by the numerical model. Therefore the question is whether other modes at different frequencies are being excited in the model that support a wave speed of about 13 m s^{-1}. To answer that question, we present in Figure 7 the spectrum obtained from a 10-day time series of the u(east) component of near-surface model-generated velocity about 30 km downstream from the forcing boundary. Note the presence of two distinct peaks, a primary peak at the forcing frequency (period of 1.5 days) and a secondary peak at twice the forcing frequency (period of 0.75 days). This demonstrates that nonlinear dynamic effects cause the model (and nature) to produce harmonics of the forcing frequency. This doubling of the forcing frequency (ω = 9.7 x 10^{-5} s^{-1}) results in secondary forcing which excites topographic waves very near the maximum allowed frequency at which the phase speed predicted by the theory is $C_x = \alpha_0 g/2fR$ = 14 m s^{-1}. This phase speed is in close agreement with the model-derived phase speed of 13 m s^{-1}.

Beyond a distance of 100 km from the forcing boundary, the model results show that the propagation regime changes to a phase velocity of $\sqrt{gH}$. Given the fact that the phase velocity is $\sqrt{gH}$ and that the disturbances travel eastward and are trapped along isobaths, the conclusion is that there is a transition to a Kelvin wave mode for distances beyond 100 km from the forcing boundary. From there on they travel northeast-

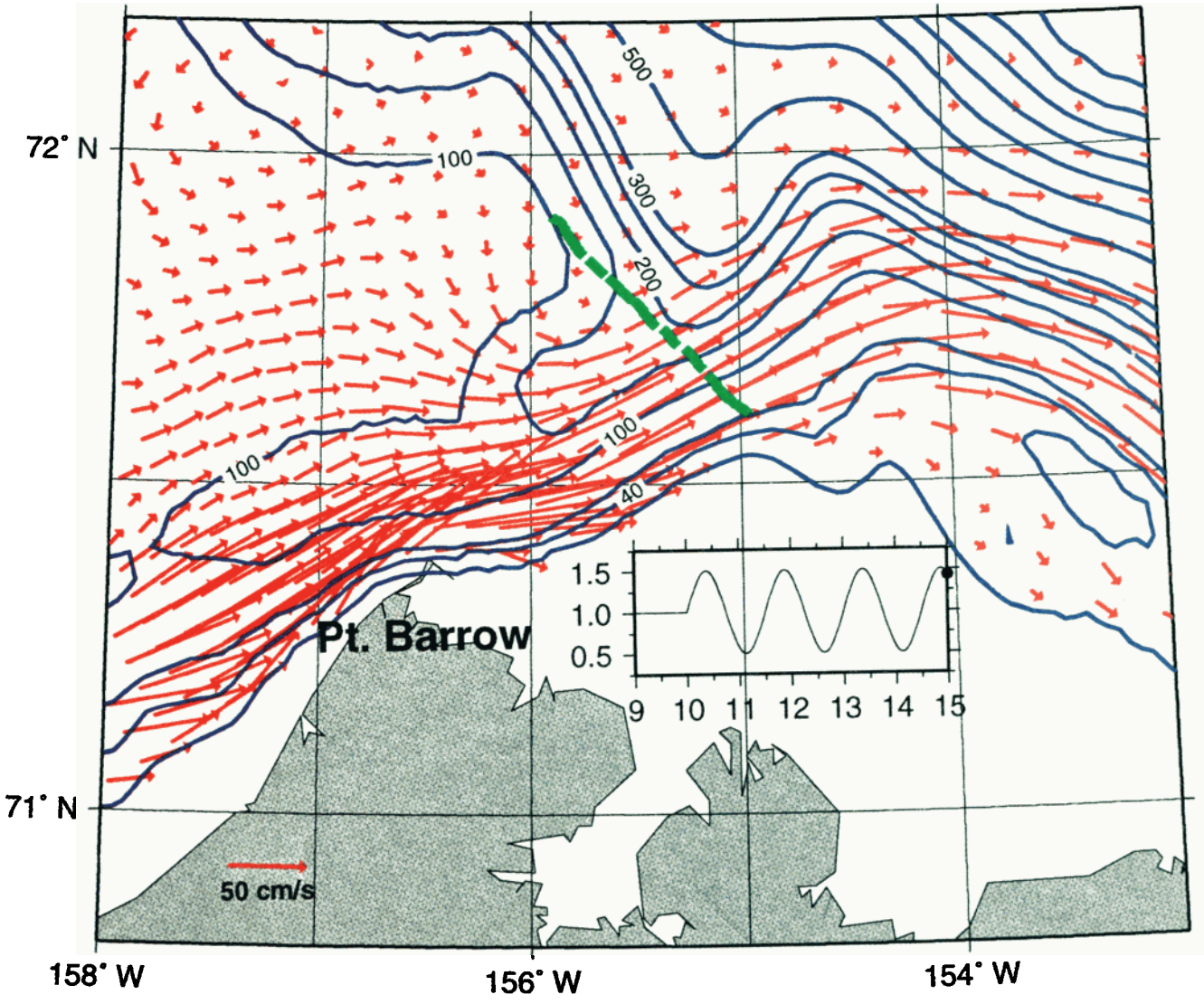

Plate 5. Snapshot (15 days after start) of model-generated velocity vectors at a depth of 30 m. The map shows a subset of grid points surrounding the ADCP survey area. At this time, the magnitude of the downcanyon velocity field generated by the model approaches that of the September 25 ADCP survey. The line of green diamonds indicates the location of the CTD transect; grid points at or closest to these points were used to produce the model-derived velocity and density transects shown in Plate 6.

ward toward the shelf break and then eastward along the shelf.

We now resume our analysis of the along-canyon momentum balance. We obtain an averaged along-canyon momentum balance by averaging its individual components across the canyon. This procedure eliminates the y dependency of the along-canyon momentum balance and results in the following momentum, density, and continuity equations:

$$\frac{\partial \bar{u}}{\partial t} + \bar{u}\frac{\partial \bar{u}}{\partial x} + \bar{w}\frac{\partial \bar{u}}{\partial z} = -f\bar{v} - \frac{1}{\rho_0}\frac{\partial \bar{p}}{\partial x} + \bar{D}_u \tag{6}$$

$$\frac{\partial \bar{\rho}}{\partial t} + \bar{u}\frac{\partial \bar{\rho}}{\partial x} + \bar{w}\frac{\partial \bar{\rho}}{\partial z} = \bar{D}_\rho \tag{7}$$

$$\frac{\partial \bar{u}}{\partial x} = -\frac{\partial \bar{w}}{\partial z} \tag{8}$$

The overbars, indicating cross-canyon averaged variables, are dropped from here on for simplicity. To further facilitate the analysis, we separate the barotropic and baroclinic components of the velocity field, and the absolute velocity is then defined as $u = U + u'$, where U is the barotropic component and u' is the baroclinic component. The barotropic velocity is calculated from the stream function as $U = -1/h\ \partial\psi/\partial y$. The cross-canyon integration introduces the following expression

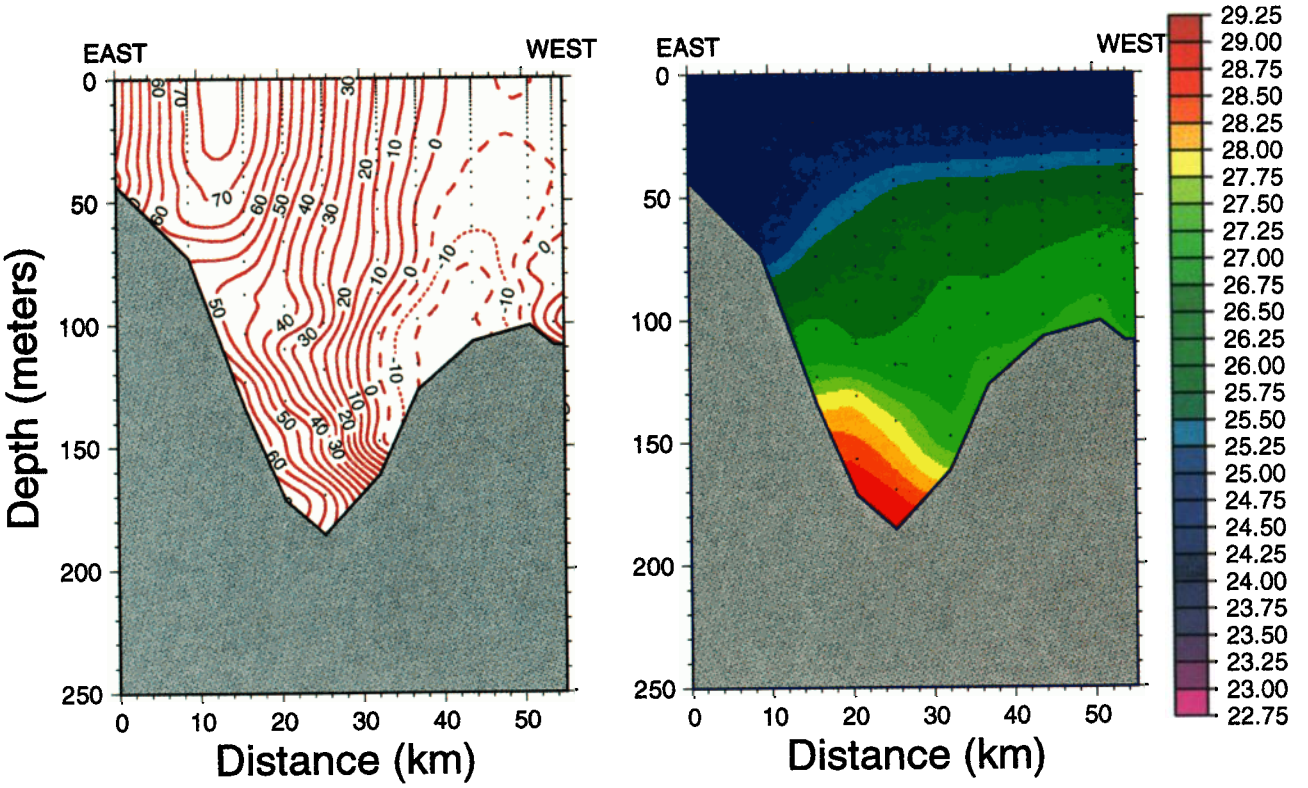

Plate 6. Model-generated (left) velocity and (right) density transect at 15 days after start. The black dots represent the location of the vertical grid points in the model.

for the cross-canyon averaged barotropic component:

$$\bar{U} = -\frac{\psi(b) - \psi(0)}{bh} = -\frac{\psi_T}{bh} \tag{9}$$

where b is the width of the jet and $\psi_T = \psi_0 + \psi_1 \sin wt$ is the cross-stream averaged time-dependent transport imposed on the southwest boundary ($\psi_0 = 1$ Sv, and $\psi_1 = 0.5$ Sv) that simulates the inflow of Bering Strait water into Barrow Canyon. After substitution of $u = u' + U$ and $w = w' + W$ in (6), invoking the continuity equation (8) and averaging over a full cycle of U, we get the following steady state cross-canyon averaged momentum equation for the along-canyon flow:

$$\frac{\partial \overline{u'u'}}{\partial x} + \frac{\partial \overline{w'u'}}{\partial z} + \frac{\partial}{\partial x}(\overline{UU}) + \frac{\partial}{\partial z}(\overline{WU}) = -fv' - \frac{1}{\rho_0}\frac{\partial p}{\partial x} + D_u \tag{10}$$

Note that there is no barotropic contribution to the Coriolis acceleration fv' because, by definition, the barotropic forcing is on the U component only. In (10) the nonlinear inertial terms associated with the sinusoidal barotropic forcing, such as $\partial/\partial x(\overline{UU})$, arise because the mean value of U^2 over a full cycle (1.5 days) is not zero. Conversely, since the forcing is a harmonic progressive wave, U and W will be 90° out of phase and the term $\partial/\partial z(\overline{WU})$ vanishes. Therefore we are left with a single steady state barotropic forcing term in (8), which is $\partial/\partial x(\overline{UU})$. This term can be analytically evaluated by invoking (9), which leads to

$$\frac{\partial}{\partial x}(\overline{UU}) = -\frac{2}{h^3}\frac{\overline{\psi_T^2}}{b^2}\frac{\partial h}{\partial x} \tag{11}$$

where $\overline{\psi_T^2} = \psi_0^2 + (1/2)\psi_1^2$.

Therefore the intensity of the steady state barotropic forcing is strongly dependent on the local depth, h, bottom slope, $\partial h/\partial x$, and the amplitude of the sinusoidal volume transport variability per unit length, $\overline{\psi_T}/b$.

We now use the model results to calculate the time average (over a 1.5-day cycle) of the u', w', and ρ fields along four cross-canyon sections. Sections 1, 2, 3, and 4 are 30, 15, 0, and -15 km upstream (southward), respectively, of the location of the central ADCP transect. Next, we calculate the cross-canyon averaged fields to construct a longitudinal transect of the steady state velocity and density fields from the model. Plate 7a shows the density field with superimposed vertical profiles of the total (barotropic and baroclinic) velocity at the four locations. Plate 7b shows the same density field, but the superimposed velocity profiles represent the baroclinic current only, that is, the depth-averaged component was individually removed. Note the strong vertical shear in these velocity profiles. The flow is characterized by a distinct middepth reversal, with the upper 80 m moving downcanyon and the lower layers (80 to 250 m) moving upcanyon. Also note that denser water ($\sigma = 28.5$) at the mouth of the canyon, normally located at a depth of 200 m, is uplifted to a depth of about 150 m and ad-

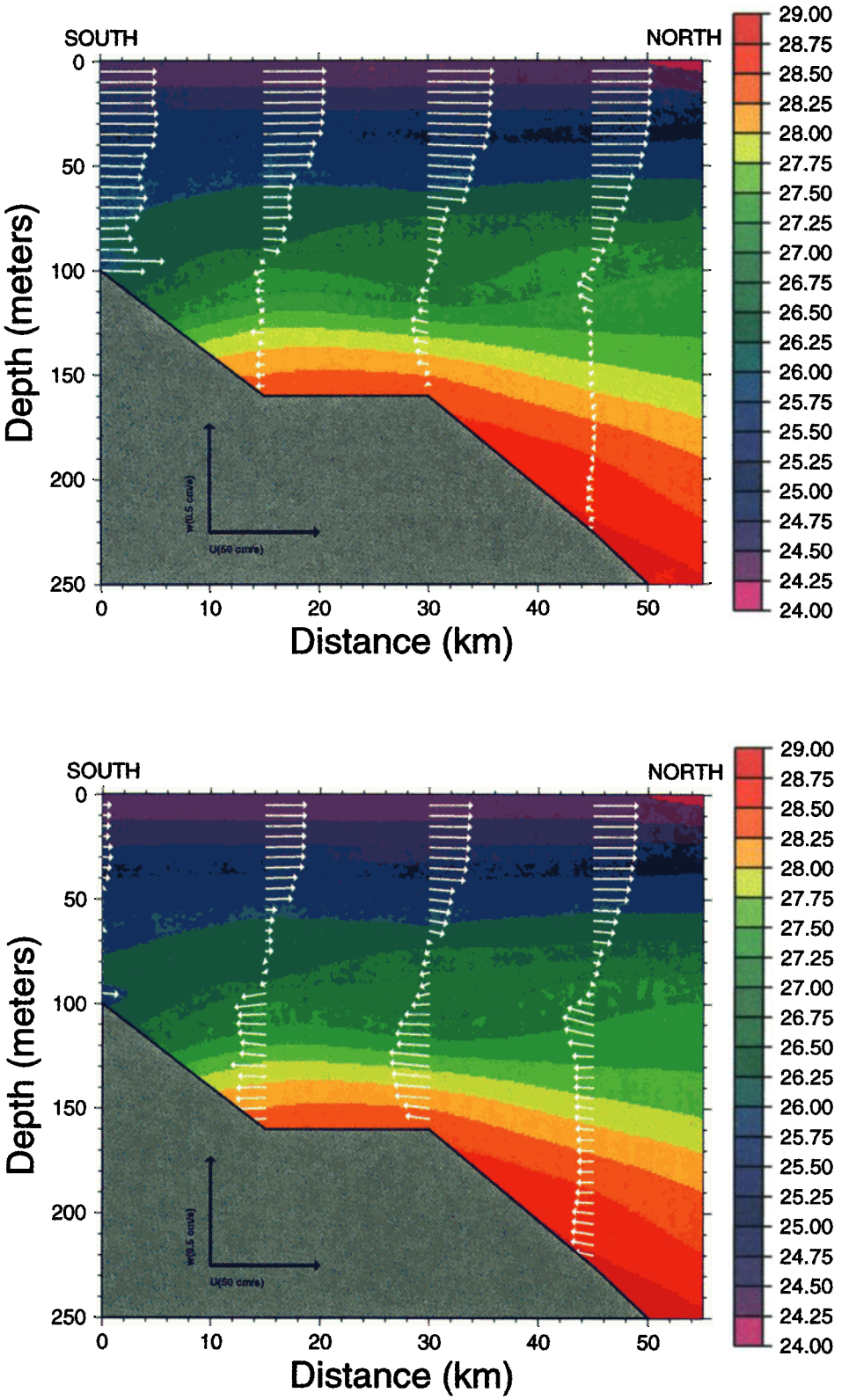

Plate 7. (a) Model-generated longitudinal density and velocity fields averaged across the coastal jet. (b) As in Plate 7a, except for baroclinic component of the longitudinal velocity field.

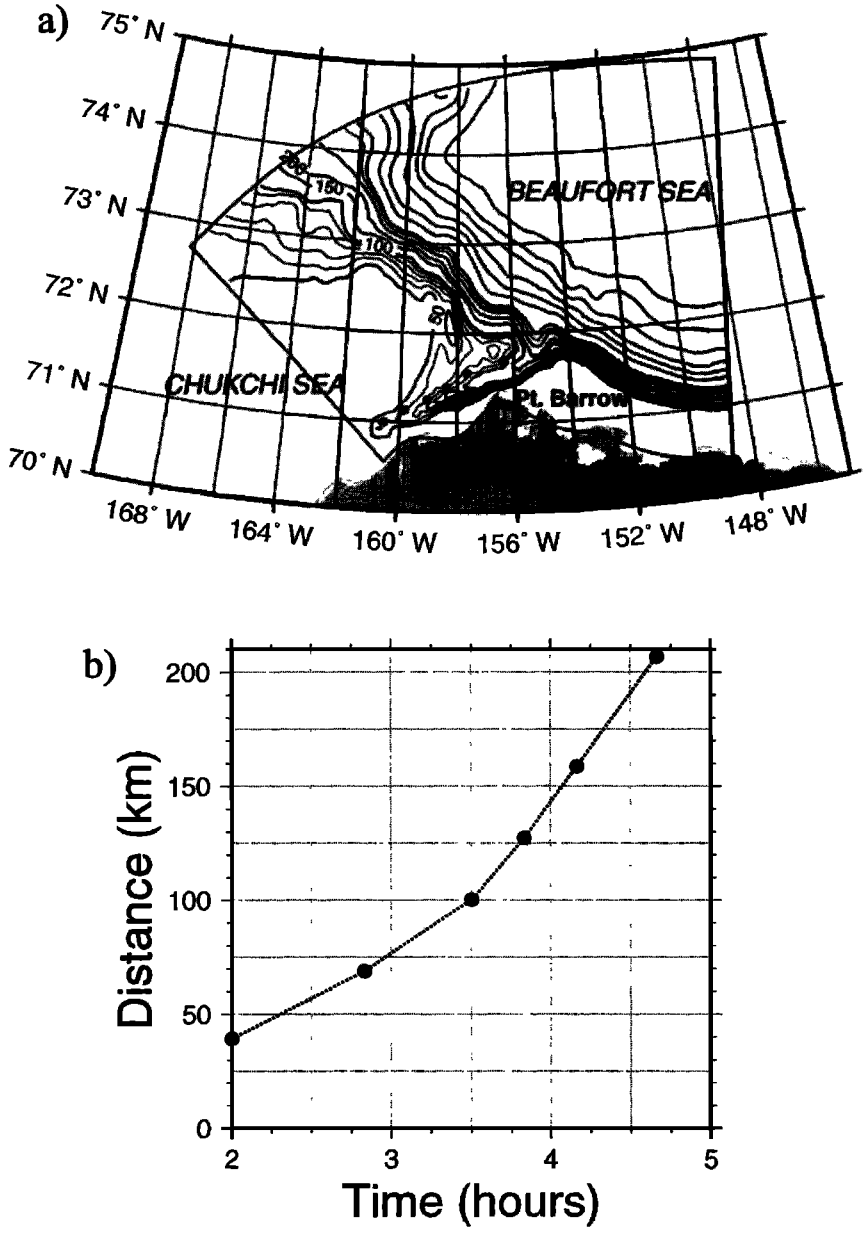

Figure 6. (a) Map of the study area showing the model grid boundaries, bathymetry, and the location of points where the phase velocity of the transport disturbance was calculated from the model output. (b) Time of arrival of maximum transport disturbance at six different locations along the coastal jet.

vects a distance of 40 km from its original downcanyon source.

To quantify the along-canyon dynamic balance, we conducted an analysis of the momentum terms shown in (10). Table 4 shows the numerical values of these terms for four different depth-averaged layers. Since the lateral and vertical viscosity coefficients needed to evaluate the viscosity terms (D_u) in the model have no observational basis for their assumed value, the viscosity terms are calculated as residuals of the dynamic balance. To evaluate the effect of $\partial/\partial x(\overline{UU})$, we chose to use sections 3 and 4 which lie over the steepest bottom slope of the cross-canyon averaged transect. Table 4 summarizes the magnitude of each term of the along-canyon momentum balance for the same four depth-averaged layers used in the cross-canyon momentum balance. The values shown in Table 4 reveal that the main dynamic balance is between the baroclinic pressure gradient, the nonlinear steady state barotropic term $\partial/\partial x(\overline{UU})$, the secondary flow Coriolis acceleration, fv', and lateral and vertical viscosity terms. The barotropic advective term is 1 order of magnitude larger than the baroclinic advective terms and the same order of magnitude as fv'. Therefore the main driving mechanism for generating the upcanyon flow is the nonlinear interaction of the variable barotropic flow with the steep bottom topography, i.e., the term shown in (11). The time derivative, $\partial u/\partial t$, accelerates the flow upcanyon and downcanyon so that the resulting momentum imbalances cause the magnitude of the inflow/outflow within the canyon to

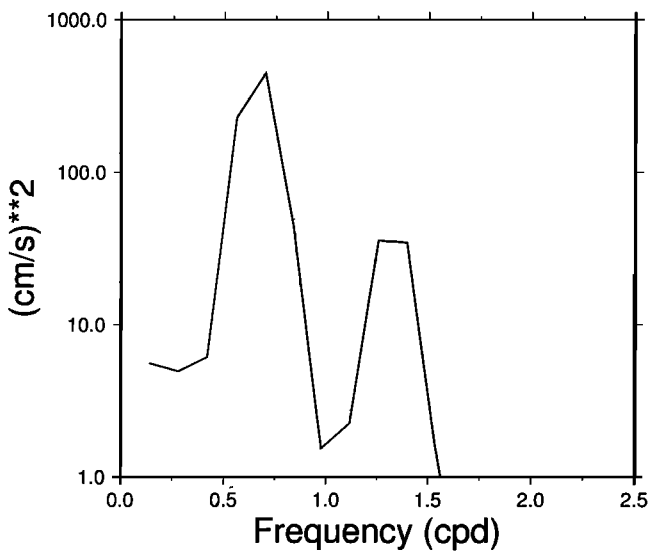

Figure 7. Power spectrum of model-generated 10-day time series of nearsurface u (east) velocity at 30 km downstream from the forcing boundary. Note the two distinct peaks, one at the forcing frequency (0.67 cpd, period of 1.5 days) and another at twice the forcing frequency (1.33 cpd, period of 0.75 day).

change accordingly. The overall effect is a rectification of the subinertial, sinusoidal volume transport disturbance. The upwelling of Atlantic water through Barrow Canyon is thus proportional to the amplitude of the transport disturbances. Upwelling is most intense during periods of large amplitude barotropic forcing. The Coriolis acceleration fv' is significant, which indicates that the secondary flow plays an important role in the momentum balance.

4. Summary and Conclusions

We conducted a dynamical investigation of the flow in Barrow Canyon using a combination of data analyses of observations and numerical simulation. The model reproduces three-dimensional dynamic balances in close agreement with balances interpreted from the data analysis. Momentum balance analyses reveal that both the baroclinic and barotropic components of the flow play a role in the dynamic balance. The cross-canyon dynamics is geostrophic, while the along-canyon dynamics is ageostrophic. Both simulated and observed fields exhibit large temporal changes of velocity and transport. The acceleration of the flow up and down the canyon is conducive to a rectified baroclinic flow having downcanyon motion within the upper layer and upcanyon motion at mid depth and below. An analysis of the along-canyon dynamic balance using simulated fields suggests that the nonlinear interaction of the variable barotropic flow with the steep topography is the primary mechanism for bringing Atlantic water to shallower depths within the canyon.

The momentum balance is geostrophic only for the barotropic cross-canyon component of the flow. The baroclinic component of the cross-canyon momentum balance is ageostrophic. Furthermore, the resulting imbalances from geostrophy generate a secondary flow with strength proportional to the vertical shear of the along-canyon flow. Although the secondary flow is small when compared with the strength of the along-canyon flow, it has significant influence on the dynamics and kinematics of the canyon regime. The transverse exchange accomplished by the secondary flow influences the structure of the along-canyon flow by changing the horizontal and vertical distributions of momentum. The density distribution across the canyon is also affected by strain field of the secondary circulation. The isopycnals in the deep pycnocline are pinched on the east side of the canyon and spread on the west side, giving the density field a wedge shape. This pattern, which is shown by both observed and modeled density fields, agrees with results of previous investigations on the effects of secondary flows on density stratification.

Our regional model of the Chukchi and Beaufort Seas provided a better dynamical understanding of the flow in and around Barrow Canyon. The results have also shown that the barotropic variability of the Bering Strait volume transport plays a significant role in the dynamics of the flow and stratification in Barrow Canyon. It is suggested that this transport variability is communicated from the Bering Strait to Barrow Canyon over the relatively shallow and gently sloping Chukchi shelf in the form of a topographic wave. Once these transport disturbances encounter the much steeper bottom topography of the canyon, there is a transition to a Kelvin wave mode of propagation. From there on they travel northwestward toward the Beaufort shelf break and then eastward trapped along isobaths. We suggest further investigation of this mechanism of propagation using a basin-scale, high-resolution barotropic (free-

Table 4. Along-Canyon Momentum Terms from Model Results

Depth Range	$\frac{\partial \overline{u'u'}}{\partial x}$	$\frac{\partial \overline{w'u'}}{\partial z}$	$-fv'$	$\frac{1}{\rho_o}\frac{\partial p}{\partial x}$	$\frac{\partial}{\partial x}(\overline{UU})$	D_u
10-30 m	0.028	0.016	0.442	0.010	-0.200	-0.297
30-70 m	0.056	-0.016	0.319	0.066	-0.200	-0.224
70-100 m	0.006	-0.058	-0.147	0.343	-0.200	-0.060
100-155 m	-0.075	-0.053	-0.269	0.699	-0.200	-0.102

Values are given in 10^{-3} cm s^{-2}. The values tabulated are averaged across the width of the canyon. The longitudinal (x component) derivatives were calculated based on transects 3 and 4, which lie over the steepest bottom slope of the canyon.

surface) model forced by the Bering Strait throughflow and winds.

Acknowledgments. We are grateful to Tom Weingartner, UAF, who provided the current meter data. We are also grateful to Kate Hedström who provided help in developing the grid for the model experiment. This study was supported by the Office of Naval Research under grants N00014-95-1-1054, N00014-93-1-0093, and N00014-94-1-0041. This work was supported in part by a grant of HPC time from the Arctic Region Supercomputing Center.

References

Aagaard, K., The Beaufort Undercurrent, in *The Alaskan Beaufort Sea: Ecosystems and Environments,* edited by P.W. Barnes et al., pp. 47-71, Academic Press, San Diego, Cal., 1984.

Aagaard, K., A synthesis of the Arctic Ocean circulation, *Rapp. P. V. Reun. Cons. Int. Explor. Mer, 188,* 11-22, 1989.

Aagaard, K., and E. C. Carmack, The role of sea ice and other fresh water in the Arctic circulation, *J. Geophys. Res., 94,* 14,485-14,498, 1989.

Aagaard, K., and E.C. Carmack, The Arctic and climate: A perspective, in *The Polar Oceans and Their Role in Shaping the Global Ocean Environment, Geophys. Monogr. Ser.,* vol. 85, edited by O.M. Johannessen, R. D. Muench, and J. E. Overland, pp. 5-20, AGU, Washington D. C., 1994.

Aagaard, K., and A.T. Roach, Arctic ocean-shelf exchange: Measurements in Barrow Canyon, *J. Geophys. Res., 95,* 18,163-18,175, 1990.

Allen, S., Topographically generated, subinertial flows within a finite length canyon, *J. Phys. Oceanogr., 26,* 1608-1632, 1996.

Coachman, L.K. and K. Aagaard, Transports through Bering Strait: Annual and interannual variability, *J. Geophys. Res., 93,* 15,535-15,539, 1988.

Coachman, L.K., and C.A. Barnes, The contribution of Bering Sea water to the Arctic Ocean, *Arctic, 16,* 9-16, 1961.

Cushman-Roisin, B., *Introduction to Geophysical Fluid Dynamics,* 320 pp., Prentice Hall, Englewood Cliffs, N. J., 1994.

D'Asaro, E.A., Generation of submesoscale vortices: A new mechanism, *J. Geophys. Res., 93,* 6685-6693, 1988a.

D'Asaro, E.A., Observations of small eddies in the Beaufort Sea, *J. Geophys. Res., 93,* 6669-6684, 1988b.

Dewey, R.K., J.N. Moum, C.A. Paulson, D.R. Caldwell, and S.D. Pierce, Structure and dynamics of a coastal filament, *J. Geophys. Res., 96,* 14,885-14,907, 1991.

Dickson, R.R., J. Meinke, S.A. Malmberg, and A. J. Lee, The "great salinity anomaly" in the northern North Atlantic, *Prog. Oceanogr., 20,* 103-151, 1988.

Eby, M., and G. Holloway, Sensitivity of a large scale ocean model to a parameterization of topographic stress, *J. Phys. Oceanogr., 24,* 2577-2588, 1994.

Freeland, H. J., and K. L. Denman, A topographically controlled upwelling center off southern Vancouver Island, *J. Mar. Res., 40,* 1069-1093, 1982.

Gawarkiewicz, G., and D. C. Chapman, A numerical study of dense water formation and transport on a shallow, sloping continental shelf, *J. Geophys. Res., 100,* 4489-4507, 1995.

Geyer, W.R., Three-dimensional tidal flow around headlands, *J. Geophys. Res., 98,* 955-966, 1993.

Haidvogel, D.B., and A. Beckmann, Numerical models of the coastal ocean, in *The Sea,* John Wiley, New York, in press, 1997.

Hedström, K.S., D. B. Haidvogel and S. R. Signorini, Model simulations of ocean/sea-ice interaction in the western Arctic in 1983, *Outer Cont. Shelf Study MMS 95-0001,* 78 pp., Alaska Outer Cont. Shelf Reg. of the Miner. Manage. Serv., U.S. Dep. of the Inter., Anchorage, Alaska, 1995.

Hickey, B., The response of a steep-sided, narrow canyon to periodic wind forcing, *J. Phys. Oceanogr., 27,* 697-726, 1997.

Holland, D.M., L. A. Mysak, and J. M. Oberhuber, An investigation of the general circulation of the Arctic Ocean using a isopycnal model, *Tellus, Ser. A, 48,* 138-157, 1996.

Johnson, G.C., and D.R. Ohlsen, Frictionally modified rotating hydraulic channel exchange and ocean outflows, *J. Phys. Oceanogr., 24,* 66-78, 1994.

Johnson, G.C., and T.B. Sanford, Secondary circulation in the Faroe Bank Channel outflow, *J. Phys. Oceanogr., 22,* 927-933, 1992.

Klinck, J.M., Geostrophic adjustment over submarine canyons, *J. Geophys. Res., 94,* 6133-6144, 1989.

Klinck, J.M., Circulation near a submarine canyon: A modeling study, *J. Geophys. Res., 101,* 1211-1223, 1996.

Kowalik, Z., and A. Y. Proshutinsky, Topographic enhancement of tidal motion in the western Barents Sea, *J. Geophys. Res., 100,* 2613-2637, 1995.

Levitus, S., T.P. Boyer, and J. Antonov, *World Ocean Atlas 1994,* vol. 4, *Temperature: NOAA Atlas NESDIS 4,* U.S. Dep. of Commer., Washington, D.C., 129 pp., 1994a.

Levitus, S., R. Burgett, and T.P. Boyer, *World Ocean Atlas 1994,* vol. 3, *Salinity: NOAA Atlas NESDIS 3,* U.S. Dep. of Commer., Washington, D.C., 111 pp., 1994b.

Manley, T.O., and K. Hunkins, Mesoscale eddies in the Arctic Ocean, *J. Geophys. Res., 90,* 4911-4930, 1985.

Melling, H., The formation of a haline shelf front in wintertime in an ice covered Arctic Sea, *Cont. Shelf. Res., 13,* 1123-1147, 1993.

Mountain, D.G., L.K. Coachman, and K. Aagaard, On the flow through Barrow Canyon, *J. Phys. Oceanogr., 6,* 461-470, 1976.

Münchow, A., and E.C. Carmack, Synoptic flow and density observations near an Arctic shelf break, *J. Phys. Oceanogr.,* in press, 1997.

Münchow, A., C.S. Coughran, M.C. Hendershott, and C.D. Winant, Performance and calibration of an acoustic Doppler current profiler towed below the surface, *J. Atmos. Oceanic Techno., 12,* 435-444, 1995.

Noble, M., and B. Butman, The structure of subtidal currents within and around Lydonia Canyon: Evidence for enhance across-shelf fluctuations over the the mouth of the canyon, *J. Geophys. Res., 94,* 8091-8110, 1989.

Paquette, R. G., and R.H. Bourke, Observations on the coastal current of Arctic Alaska, *J. Mar. Res., 32,* 195-207, 1974.

Rosenfeld, L.K., F.B. Schwing, N. Garfield, and D.N. Tracy, Bifurcated flow from an upwelling center: A cold water source for Monterey Bay, *Cont. Shelf. Res., 14,* 931-964, 1994.

Song Y., and D. Haidvogel, A semi-implicit ocean circulation model using a generalized topography-following coordinate system, *J. Comput. Phys., 115,* 228-244, 1994.

D. Haidvogel and A. Münchow, Institute of Marine and Coastal Sciences, Rutgers University, Cook Campus, New Brunswick, NJ 08903.

S.R. Signorini, General Sciences Corporation, 6100 Chevy Chase Drive, Suite 200, Laurel, MD 20707. (e-mail: sergio@mrslate.gsc.saic.com)

(Received June 28, 1996; revised February 19, 1997; accepted March 5, 1997.)